Analysis and improvement of motion encoding in magnetic resonance elastography

Guenthner, Christian ; Runge, Jurgen Henk ; Sinkus, Ralph ; Kozerke, Sebastian

Abstract: Magnetic resonance elastography (MRE) utilizes phase contrast magnetic resonance imaging (MRI), which is phase locked to externally generated mechanical vibrations, to measure the three-dimensional wave displacement field. At least four measurements with linear-independent encoding directions are necessary to correct for spurious phase contributions if effects from imaging gradients are non-negligible. In MRE, three encoding schemes have been used: unbalanced four- and six-point and balanced four-point ('tetrahedral') encoding. The first two sensitize to motion with orthogonal gradients, with the four-point method acquiring a single reference scan without motion sensitization, whereas three additional scans with inverted gradients are used with six-point encoding, leading to two-fold higher displacement-to-noise ratio (DNR) and 50% longer scan duration. Balanced four-point (tetrahedral) encoding encodes along the four diagonals of a cube, with one direction serving as a reference for the other three encoding directions, similar to four-point encoding. The objective of this work is to introduce a theoretical framework to compare different motion sensitization strategies with respect to their motion encoding efficiency in two fundamental encoding limits, the gradient strength limit and the dynamic range limit, which are both placed in relation to conventional gradient recalled echo (GRE)- and spin echo (SE)-based MRE sequences. We apply the framework to the three aforementioned schemes and show that the motion encoding efficiency of unbalanced four- and six-point encoding schemes in the gradient-limited regime can be increased by a factor of 1.5 when using all physical gradient channels concurrently. Furthermore, it is demonstrated that reversing the direction of the reference in balanced four-point (tetrahedral) encoding results in the Hadamard encoding scheme, which leads to increased DNR by 2 compared with balanced four-point encoding and 2.8 compared with unbalanced four-point encoding. As an example, we show that optimal encoding can be utilized to reduce the acquisition time of standard liver MRE in vivo from four to two breath holds.

DOI: https://doi.org/10.1002/nbm.3908

Guenthner, Christian; Runge, Jurgen Henk; Sinkus, Ralph; Kozerke, Sebastian (2018). Analysis and improvement of motion encoding in magnetic resonance elastography. NMR in Biomedicine, 31(5):e3908. DOI: https://doi.org/10.1002/nbm.3908

Received: 22 August 2017 | Revised: 12 January 2018 | Accepted: 22 January 2018

DOI: 10.1002/nbm.3908

RESEARCH ARTICLE

WILEY NMR IN BIOMEDICINE

Analysis and improvement of motion encoding in magnetic resonance elastography

Christian Guenthner[1] | Jurgen Henk Runge[2,3] | Ralph Sinkus[2] | Sebastian Kozerke[1]

[1] Institute for Biomedical Engineering, University and ETH Zurich, Zurich, Switzerland

[2] Division of Imaging Sciences & Biomedical Engineering, King's College London, London, UK

[3] Radiology and Nuclear Medicine, Academic Medical Center, Amsterdam, the Netherlands

Correspondence
C. Guenthner, Institute for Biomedical Engineering, University and ETH Zurich, 8092 Zurich, Switzerland.
Email: guenthner@biomed.ee.ethz.ch

Funding information
European Union's Horizon 2020 research and innovation programme, Grant/Award Number: 668039

Magnetic resonance elastography (MRE) utilizes phase contrast magnetic resonance imaging (MRI), which is phase locked to externally generated mechanical vibrations, to measure the three-dimensional wave displacement field. At least four measurements with linear-independent encoding directions are necessary to correct for spurious phase contributions if effects from imaging gradients are non-negligible. In MRE, three encoding schemes have been used: unbalanced four- and six-point and balanced four-point ('tetrahedral') encoding. The first two sensitize to motion with orthogonal gradients, with the four-point method acquiring a single reference scan without motion sensitization, whereas three additional scans with inverted gradients are used with six-point encoding, leading to two-fold higher displacement-to-noise ratio (DNR) and 50% longer scan duration. Balanced four-point (tetrahedral) encoding encodes along the four diagonals of a cube, with one direction serving as a reference for the other three encoding directions, similar to four-point encoding. The objective of this work is to introduce a theoretical framework to compare different motion sensitization strategies with respect to their motion encoding efficiency in two fundamental encoding limits, the gradient strength limit and the dynamic range limit, which are both placed in relation to conventional gradient recalled echo (GRE)- and spin echo (SE)-based MRE sequences. We apply the framework to the three aforementioned schemes and show that the motion encoding efficiency of unbalanced four- and six-point encoding schemes in the gradient-limited regime can be increased by a factor of 1.5 when using all physical gradient channels concurrently. Furthermore, it is demonstrated that reversing the direction of the reference in balanced four-point (tetrahedral) encoding results in the Hadamard encoding scheme, which leads to increased DNR by $\sqrt{2}$ compared with balanced four-point encoding and 2.8 compared with unbalanced four-point encoding. As an example, we show that optimal encoding can be utilized to reduce the acquisition time of standard liver MRE *in vivo* from four to two breath holds.

Abbreviations used: BW, readout bandwidth; DFT, discrete Fourier transform; DNR, displacement-to-noise ratio; DynR, dynamic range limit; EPI, echo planar imaging; Grad, gradient strength limit; GRE-MRE, gradient recalled echo-based MRE; IVPD, intra-voxel phase dispersion; M,P,S, measurement, phase, slice encoding direction coordinate system; MD-RME, multidirectional reduced motion encoding; MEG, motion encoding gradient; MRE, magnetic resonance elastography; MRI, magnetic resonance imaging; ROI, region of interest; SE-MRE, spin echo-based MRE; SENSE, sensitivity encoding; SLIM, sample interval modulation; SNR, signal-to-noise ratio; TE, echo time; TR, repetition time; TTL, transistor-transistor logic; *XYZ*, gradient coordinate system.

Symbols: $B_0(\vec{x})$, magnetic field inhomogeneity map; cov, covariance matrix; $\vec{d}, g(t), G$, motion encoding gradient (MEG) direction, gradient wave form, gradient strength; $\widehat{E}, \widehat{D}, N_{\mathrm{Enc}}$, encoding matrix, decoding matrix, number of encoding directions; $\widehat{e}_m, g_m(t), G_m$, unit vector of imaging coordinate system, gradient wave form, gradient strength; $\mathcal{F}$, discrete Fourier transformation; $\vec{G}$, gradient field; N_{P}, k, number of mechanical phase offsets, mechanical phase index; ϵ_f, $\epsilon_{m,\,f}$, encoding efficiency (MEG), encoding efficiency of imaging gradients; $\vec{r}, f, \theta$, wave displacement, frequency, phase; r_{enc}, maximal displacement without phase wrap (dynamic range); Γ, imaging gradients to MEG encoding ratio; ζ, encoding efficiency in relation to unbalanced four-point encoding; η, σ_η, random variable for phase noise, standard deviation of phase noise; ϕ_k, δ_k, motion phase (MEG), spurious phase contribution from imaging gradients; $\varphi_{i,\,k}$, image phase with motion encoding along the ith encoding direction; Ω, ϕ_r, ϕ_R, dynamic range region, dynamic range radius, circumscribed sphere radius.

The copyright line for this article was changed on 31 January 2019 after original online publication.

KEYWORDS

encoding efficiency, four-point encoding, Hadamard encoding, magnetic resonance elastography, tetrahedral encoding

1 | INTRODUCTION

Magnetic resonance elastography (MRE) allows the *in vivo* determination of local tissue shear stiffness using time-resolved measurements of shear wave-induced signal phase shifts.[1] Recent technological advances in the field have focused on the development of actuator systems,[2-5] wave inversion algorithms,[6-9] improved image acquisition[10,11] and motion encoding techniques.[12-15]

Fundamentally, a key metric for the optimization of MRE is the displacement-to-noise ratio (DNR). DNR itself depends on the signal-to-noise ratio (SNR) and the amount of phase shift generated per unit tissue displacement. In a practical setting and for a given sequence, optimization of DNR involves finding a suitable trade-off between spatial resolution and scan duration. Frequently, DNR is increased by averaging multiple measurements (N_{avg}) or by acquiring more than three mechanical phase offsets.[12,15,16] This approach leads to an increase in DNR by $\sqrt{N_{avg}}$, whereas the scan time is proportional to N_{avg}. In order to increase DNR without changing the scan duration, higher motion encoding efficiency through increased gradient strength and duration can be achieved. However, gradient amplifiers and the duty cycle limit the applicable gradient strength and duration. In addition, sequence timing constraints determine the maximum number of gradient cycles as well as the frequency relative to the measured wave.

Another way of increasing DNR in MRE is to change the applied motion encoding scheme. In order to correct for spurious phase contributions from imaging gradients, which are especially present in gradient recalled echo-based MRE (GRE-MRE), at least four measurements with different gradient directions are needed when acquiring the full three-dimensional displacement field. In MRE, two encoding schemes are prominently used. Unbalanced four-point encoding encodes along three orthogonal encoding directions and corrects for imaging gradients by the measurement of a single reference phase image without motion sensitization.[12,17-19] Six-point encoding inverts each motion encoding gradient (MEG) to pairwise correct for imaging gradient offsets, thereby increasing DNR by two-fold at the cost of a 50% longer scan duration compared with unbalanced four-point encoding.[11,18,20,21] A non-orthogonal balanced four-point encoding scheme has also been reported and is referred to as 'tetrahedral encoding', which encodes along the four diagonals of a regular cube. Here, a reference scan with simultaneous motion encoding along all three encoding directions is acquired and, in the subsequent three measurements, one gradient direction at a time is inverted. Accordingly, in tetrahedral encoding, the motion phase is decoded by subtraction of the reference from each encoded direction, comparable with unbalanced four-point encoding.[22] As two measurements with inverted motion sensitization are subtracted, the DNR increase is equivalent to six-point encoding. The latter scheme, however, can lead to non-integer phase wraps when the accumulated motion phases exceed the dynamic range.[23] Especially, in spin echo-based MRE (SE-MRE) sequences, the long echo times (TEs) usually permit full-wave encoding with multiple MEG repetitions leading to a high encoding efficiency. Here, the dynamic range can easily be reached or exceeded, leading to phase wraps (dynamic range limit), which need to be corrected for. On the other hand, GRE-MRE sequences typically have short TEs and utilize fractional encoding to balance the motion encoding efficiency and SNR loss as a result of T_2^* signal decay, which typically results in displacements being encoded without phase wrapping, but also with low efficiency (gradient-limited regime).

In addition to conventional sampling using equidistant phase offsets and sequential sampling of encoding directions and phases, encoding concepts utilizing temporally shifted MEGs with the simultaneous acquisition of multiple encoding directions, e.g. sample interval modulation (SLIM) and multidirectional reduced motion encoding (MD-RME), have been proposed recently.[14,24] SLIM encodes each motion component by varying the sampling interval to project each encoding direction to a different frequency, allowing the acquisition of the full motion field with only eight instead of 24 measurements. However, the original suggestion of only temporally shifting the MEGs necessitates prolonged TEs to freely shift the MEGs within 1.875 wave periods.[14] MD-RME utilizes a similar concept to SLIM, but was designed using a framework for optimization-based sequence design for MRE. Here, a linear model and the application of optimization theory allow for the simultaneous optimization of both temporal and directional encoding. The 'optimal' MD-RME scheme is similar to SLIM, but only 1.25 wave periods are necessary for temporal shifting of the MEGs, mitigating the overall TE increase.[24] Both SLIM- and MD-RME-MRE can be classified as part of the reference-less motion encoding schemes, a fourth category of encoding schemes that uses only three orthogonal motion encoding directions. Both schemes, however, neglect the influence of imaging gradients on the encoded motion field and can thus only be applied in carefully designed SE-MRE sequences, where the influence of imaging gradients is negligible. In GRE-MRE, however, imaging gradients cannot be neglected and necessitate the use of at least four encoding directions.

The objective of this work is to propose a theoretical framework for comparison of different motion encoding strategies in terms of their motion encoding efficiency and dynamic range in conventional MRE, where encoding directions and phases are acquired sequentially. The influence of imaging gradients is investigated and taken into consideration, allowing the application of the findings to both SE- and GRE-based conventional MRE sequences, which constitute the majority of contemporary four-dimensional MRE protocols. In addition, dynamic range considerations allow for the prediction of phase wrapping, which is crucial for experiment design. It is demonstrated that the motion encoding efficiency of unbalanced four- and six-point encoding schemes in the gradient-limited regime can be increased by a factor of 1.5 when using all physical gradient channels concurrently. Moreover, we propose Hadamard encoding,[23,25-27] providing up to 2.8-fold increase in encoding efficiency relative to the unbalanced four-point scheme. As an example, we show that optimal encoding can be utilized to reduce the acquisition time of a standard liver MRE *in vivo* from four to two breath holds.

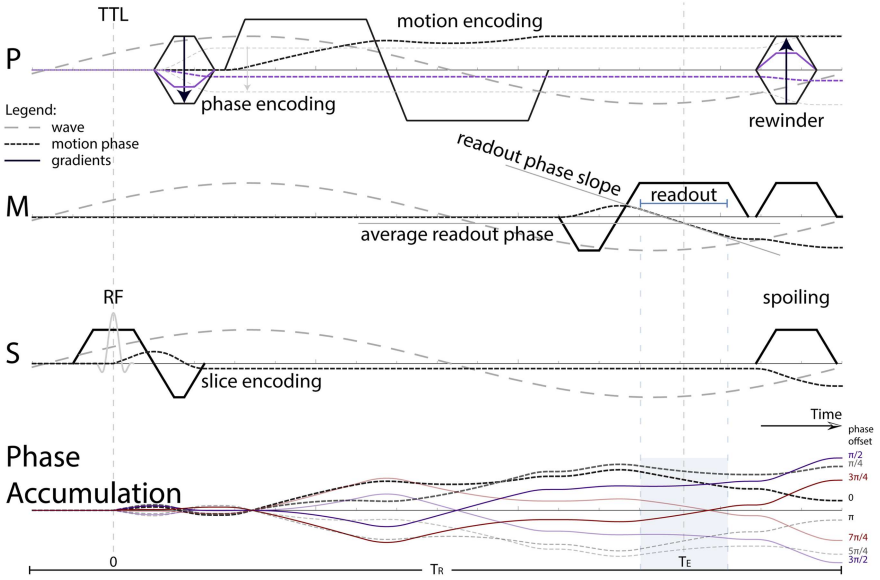

FIGURE 1 Pulse diagram of one repetition of a typical phase-locked gradient recalled echo-based magnetic resonance elastography (GRE-MRE) sequence showing excitation, motion encoding, imaging gradients and spoilers. Gradients are not to scale and are offset for visual guidance and to emphasize their phase contributions. Gradients are displayed as full lines, the broken gray sinusoid denotes the wave and the broken black lines show the contributions of the different imaging and motion encoding gradients (MEGs). Motion sensitization is assumed to be in the P direction. In addition to the MEG, imaging gradients contribute to the motion phase. Contributions which are constant over the wave period, i.e. the synchronization of the sequence and the wave generator, can be neglected. Variable contributions are: (1) the slice selection and readout gradients cause a phase offset; (2) the readout gradient causes an additional gradient of the phase during the readout, which is approximately linear if the bandwidth is much larger than the wave frequency; and (3) the phase encoding gradient causes a phase offset proportional to *ky* (violet line). RF, radiofrequency; TE, echo time; TR, repetition time; TTL, transistor-transistor logic

2 | THEORY

An example of a GRE-MRE sequence with fractional encoding is depicted in Figure 1. The phase induced by spin displacement due to the MEG in the phase encoding direction (P) is shown as a black broken line in the graph. In addition to the MEG-induced phase, imaging gradients also encode periodic motion. Their 'spurious' phase contributions can be grouped into three parts. (a) The slice selection (S) and readout (M) gradients cause an additional phase offset. (b) The readout gradient leads to an additional gradient of the phase during the readout, which is approximately linear if the bandwidth is much larger than the wave frequency. (c) The phase encoding gradient results in a phase offset, which is proportional to the phase encoding step k_y, with no net phase contribution in the *k*-space center. Hence, it can be treated analogously to the phase gradient of the readout gradient.

In the following, the correction of phase offsets of type (a) are treated. Phase offsets of type (b) and (c) will be discussed shortly at the end of the Theory section.

Let us assume that spins are subject to a mono-frequency wave in steady state. Each spin thus undergoes periodic sinusoidal motion of the form

$$\vec{r}_k\left(\vec{x},t\right) = \vec{r}_0\left(\vec{x}\right)\sin\left(2\pi ft + \theta\left(\vec{x}\right) + 2\pi N_P^{-1}k\right), \tag{1}$$

where $\vec{r}_0\left(\vec{x}\right)$ is the local displacement amplitude, f is the frequency of the wave, $\theta\left(\vec{x}\right)$ is the local wave phase, N_P is the number of mechanical phase offsets acquired and k is the index of the phase offset. The accumulated phase caused by an external gradient field $\vec{G}(\tau)$ is then given by the integral[28,29]

$$\phi\left(\vec{x},t\right) = \gamma\int_0^t d\tau\,\vec{r}\left(\vec{x},\tau\right)\vec{G}(\tau). \tag{2}$$

The gradient field $\vec{G}(\tau)$ can be split into two contributions, imaging gradients (index I), $\vec{G}_I(\tau) = \sum_{m\in\{M,P,S\}} G_m\hat{e}_m g_m(\tau)$, such as the slice encoding or measurement gradient, and the MEG, $\vec{G}_{MEG}(\tau) = G\,\vec{d}\;g(\tau)$ (index MEG). Both are assumed to be separable into a time-dependent waveform $g(t)$, a constant direction of the gradient field $\vec{d}$ or the three basis vectors $\hat{e}_m$ of the MPS coordinate system (index m), and the maximal strength per gradient channel G. Including local magnetic field inhomogeneities $B_0\left(\vec{x}\right)$, but neglecting effects such as concomitant fields or eddy currents, the total acquired image phase at TE can be written as

$$\varphi_{i,k}\left(\vec{x}\right) = \underbrace{\gamma B_0\left(\vec{x}\right)\mathrm{TE} + \mathrm{Im}\left[\sum_{m\in\{\mathrm{M,P,S}\}}\left(\hat{e}_m\cdot\vec{r}_0\left(\vec{x}\right)e^{i\theta\left(\vec{x}\right)}\right)\left(G_m\epsilon_{m,f}e^{i\tilde{\theta}_{m,f}}\right)e^{i2\pi\frac{k}{N_p}}\right]}_{=\delta_k\left(\vec{x}\right)\quad(\text{"spurious contribution"})} + \vec{d}_i\cdot\underbrace{\mathrm{Im}\left[\left(\vec{r}_0\left(\vec{x}\right)e^{i\theta\left(\vec{x}\right)}\right)\left(G\epsilon_f e^{i\tilde{\theta}_f}\right)e^{i2\pi\frac{k}{N_p}}\right]}_{=\vec{\phi}_k\left(\vec{x}\right)} + \eta. \tag{3}$$

Here, the magnitude of the encoding efficiency ϵ_f is given by

$$\epsilon_f = \gamma\left|\int_0^{\mathrm{TE}} d\tau g(\tau)e^{i2\pi\tau f}\right|. \tag{4}$$

Depending on the gradient waveform, the periodic motion is encoded with a phase offset $\tilde{\theta}_f$ and $\tilde{\theta}_{m,f}$, which is constant, but frequency and gradient waveform dependent. η is a random variable added to account for phase noise. The phase noise is assumed to be uncorrelated with zero mean and standard deviation $\sigma_\eta = \mathrm{SNR}^{-1}$, where SNR is the SNR of the underlying magnitude image.[30,31] The first two summands are spurious contributions $\delta_k\left(\vec{x}\right)$, which need to be accounted for in order to determine the motion phase $\vec{\phi}_k\left(\vec{x}\right)$.

As the problem is linear and δ_k does not contain a dependence on the direction $\vec{d}_i$ of the MEG, four measurements suffice to determine the three motion phase components as well as the spurious offset. We can define an encoding matrix $\hat{E}$, whose rows denote the different measurements i and columns denote the encoding directions $\vec{d}_i$, as well as the spurious phase δ_k. Then, Equation 3 can be rewritten as

$$\vec{\varphi}_k\left(\vec{x}\right) = \hat{E}\begin{pmatrix}\vec{\phi}_k\left(\vec{x}\right)\\ \delta_k\left(\vec{x}\right)\end{pmatrix} + \vec{\eta}\,. \tag{5}$$

A noise optimal solution of this equation can be found using the Moore-Penrose pseudo-inverse $\hat{D} = \mathrm{pinv}\left(\hat{E}\right)$, which will be referred to as the decoding matrix.[32]

Given that the motion phases $\vec{\phi}_k\left(\vec{x}\right)$ are determined, a discrete Fourier transform (DFT) is used to extract the local spin displacement $\vec{r}_0\left(\vec{x}\right)$ as well as the wave delay $\theta\left(\vec{x}\right)$.[17,33] Insertion of $\vec{\phi}_k\left(\vec{x}\right)$ into the DFT leads to

$$\frac{2}{N_\mathrm{P}}\sum_{k=1}^{N_\mathrm{P}}\vec{\phi}_k\left(\vec{x}\right)e^{-i\frac{2\pi k}{N_\mathrm{P}}} = -i\left(\vec{r}_0\left(\vec{x}\right)e^{i\theta\left(\vec{x}\right)}\right)\left(G\epsilon_f e^{i\tilde{\theta}_f}\right). \tag{6}$$

As an arbitrary phase offset can be neglected and the waveform $g(t)$ is not changed during an MRE experiment (hence $\tilde{\theta}_f$ is constant), the displacement and wave delay are directly given by

$$\vec{r}_0\left(\vec{x}\right)e^{i\theta\left(\vec{x}\right)} = \frac{2}{N_\mathrm{P}G\epsilon_f}\sum_{k=1}^{N_\mathrm{P}}\vec{\phi}_k\left(\vec{x}\right)e^{-i\frac{2\pi k}{N_\mathrm{P}}}. \tag{7}$$

2.1 | Properties of encoding and decoding

2.1.1 | Noise covariance

Under the assumption of uncorrelated noise η with zero mean and standard deviation σ_η, the covariance matrix of the reconstructed phases $\hat{D}\cdot\vec{\varphi}_k\left(\vec{x}\right)$ can be shown to be given by (Appendix A)

$$\mathrm{cov} = \sigma_\eta^2\left(\hat{D}\hat{D}^\mathrm{T}\right) = \begin{pmatrix}\sigma_x^2 & c_{xy} & c_{xz} & c_{x\delta}\\ c_{xy} & \sigma_y^2 & c_{yz} & c_{y\delta}\\ c_{xz} & c_{yz} & \sigma_z^2 & c_{z\delta}\\ c_{x\delta} & c_{y\delta} & c_{z\delta} & \sigma_\delta^2\end{pmatrix}. \tag{8}$$

Here, the diagonal elements denote the variance of the noise in the motion and the spurious phase, whereas the off-diagonal elements contain their correlations. For symmetrical encoding schemes, i.e. schemes that encode motion along all coordinates equally, the covariance matrix is simplified to

$$\mathrm{cov} = \sigma_\eta^2\left(\widehat{D}\widehat{D}^\mathsf{T}\right) = \begin{pmatrix} \sigma^2 & c & c & c_\delta \\ c & \sigma^2 & c & c_\delta \\ c & c & \sigma^2 & c_\delta \\ c_\delta & c_\delta & c_\delta & \sigma_\delta^2 \end{pmatrix}, \tag{9}$$

and hence the standard deviation σ and covariance c suffice to fully describe the noise of the decoded motion phases. This is the case for all presented schemes in this work.

2.1.2 | Dynamic range

A scheme's dynamic range denotes the domain Ω of motion phases $\vec{\phi}$ for which encoding, phase wrapping and subsequent decoding yield the same motion phase, i.e.

$$\forall\,\vec{\phi}\in\Omega\colon \vec{\phi} = \widehat{D}\arg\left(\exp\left(\mathrm{i}\widehat{E}\vec{\phi}\right)\right). \tag{10}$$

It should be noted that it is assumed that no phase unwrapping technique is applied prior to decoding (see Discussion). Neglecting the influence of the imaging gradient offset phase δ_k on the encoding, Ω becomes a subspace of $\mathbb{R}^3$, and the problem can be visualized as a three-dimensional region plot. To quantify the dynamic range, multiple properties can be computed. The inscribed sphere around the origin $\vec{0}$ with radius ϕ_r depicts the maximal motion phase that can be encoded in any direction without wrapping. It is determined by

$$\pi = \left\|\vec{d}\right\|_2 \phi_r, \tag{11}$$

where $\left\|\vec{d}\right\|_2$ denotes the maximal applied MEG strength of the scheme in units of the per channel gradient strength G. This will commonly be referred to as the dynamic range of the scheme. Another property is the radius of the circumscribed sphere ϕ_R, which refers to the maximal phase without wrap in one specific direction. In Figure 2(A), the dynamic range regions, as well as in- and circumscribed spheres, are displayed for unbalanced four-point and Hadamard encoding assuming that the spurious phase offset δ_k is negligible.

Taking the gradient strength and encoding efficiency into account, the dynamic range can also be expressed in terms of the maximal displacement, which is given by

$$r_{\mathrm{enc}} = \frac{\phi_r}{\epsilon_f G}. \tag{12}$$

This is equivalent to v_{enc} of flow encoding.[23] If displacements exceed the dynamic range radius, phase wrapping occurs.

Incorporating the imaging gradient phase offset into the dynamic range region Ω yields a four-dimensional region, which again can be characterized by its inscribing four-dimensional hyper-sphere. As field inhomogeneity and concomitant fields are constant with respect to the acquired mechanical phase offsets, they can be filtered out prior to decoding and can be neglected in the dynamic range analysis. The offset phase δ_k is bounded by

$$\left|\delta_k\left(\vec{x}\right)\right| \le \left\|r_0\left(\vec{x}\right)\right\|_2 \sqrt{\sum_m \left(G_m\epsilon_{m,f}\right)^2} \le \underbrace{\frac{\sqrt{\sum_m \left(G_m\epsilon_{m,f}\right)^2}}{G\epsilon_f}}_{=\Gamma}\phi_r, \tag{13}$$

where Γ is the imaging gradient to MEG encoding efficiency ratio. Hence, it is best to formulate the dynamic range problem in spherical coordinates, yielding

$$\phi\begin{pmatrix} \sin\alpha\sin\beta \\ \sin\alpha\cos\beta \\ \cos\alpha \\ \Gamma \end{pmatrix} = \widehat{D}\arg\left(\exp\left(\mathrm{i}\widehat{E}\phi\begin{pmatrix} \sin\alpha\sin\beta \\ \sin\alpha\cos\beta \\ \cos\alpha \\ \Gamma \end{pmatrix}\right)\right). \tag{14}$$

The dynamic range $\phi_r(\Gamma)$ is then given by the maximal radius ϕ of the four-dimensional hyper-sphere, for which all radii smaller than $\phi_r(\Gamma)$ fulfill Equation 14 independent of the angles α and β. The six schemes (Table 1) all share the same dynamic range dependence, which is given by

$$\pi = \left(\left\|\vec{d}\right\|_2 + \Gamma\right)\phi_r(\Gamma) \Leftrightarrow \phi_r(\Gamma) = \frac{\phi_r}{1+\frac{\Gamma\phi_r}{\pi}}, \tag{15}$$

where ϕ_r denotes the dynamic range radius without taking imaging gradients into account. In Figure 2(B), the three-dimensional projection of the dynamic range region of Hadamard encoding for a fixed encoding efficiency ratio Γ = 0.4 is shown, together with its inscribing sphere of radius

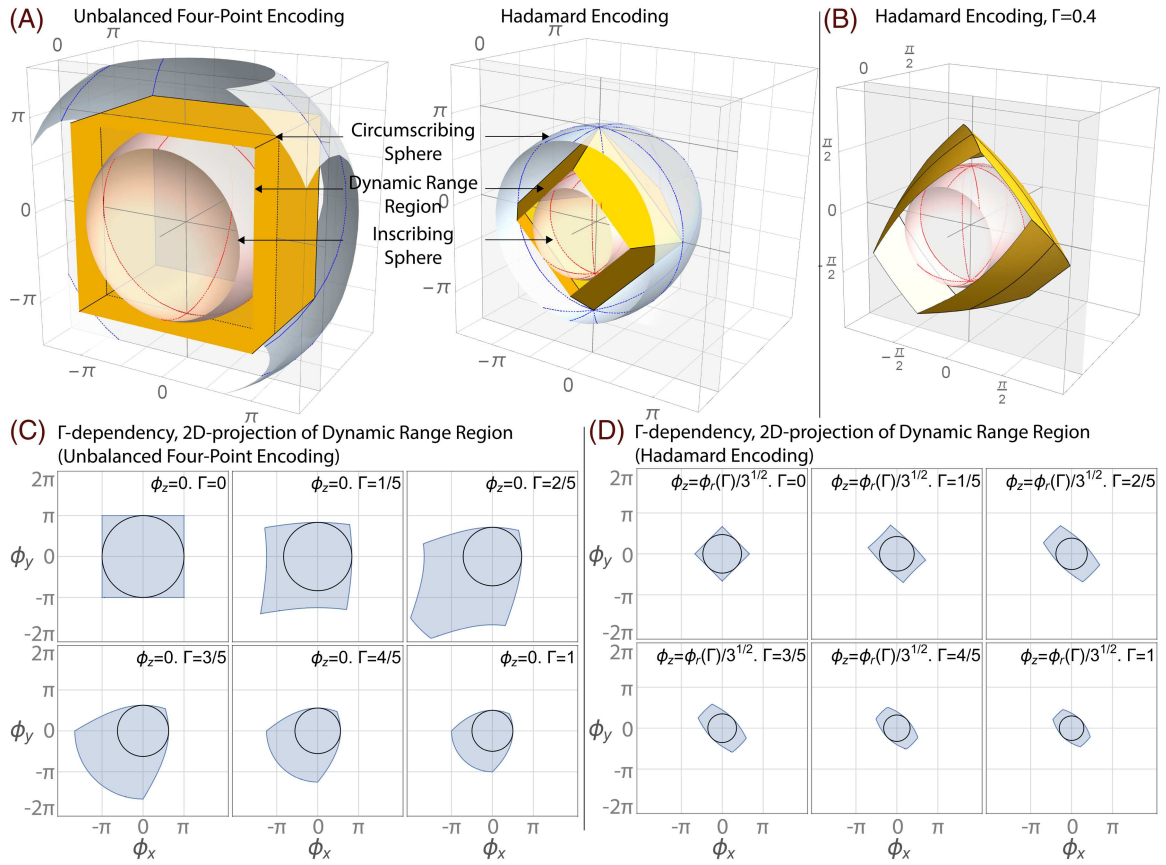

FIGURE 2 (A) Dynamic range visualization for the unbalanced four-point and Hadamard encoding schemes assuming that phases due to imaging gradients and magnetic field inhomogeneity are negligible. The orange box denotes the boundary of the dynamic range region. The gray sphere indicates the maximal encoded phase without phase wrap and the inscribing sphere in red depicts the maximal motion phase in any direction. (B) Inclusion of imaging gradients into the dynamic range determination leads to shrinking and skewing of the dynamic range region as shown for Hadamard encoding and imaging to motion encoding gradient (MEG) encoding ratio Γ of 0.4 (for definition, see Equation 13). (C, D) Two-dimensional projections of the four-dimensional dynamic range regions for six different values of Γ and respective in-circle projections. In general, a small dynamic range region is a manifestation of the high motion sensitivity of the encoding scheme

$\phi_r(\Gamma)$. The dynamic range regions deform and shrink with increasing Γ. In Figure 2(C,D), this behavior is plotted for both unbalanced four-point and Hadamard encoding in terms of projections of the four-dimensional regions. In both cases, the projection plane was chosen to be orthogonal to $(0\ 0\ 1\ 1)^T$ and intercepted the point $(0\quad 0\quad 0\quad \Gamma)^T$ for unbalanced four-point encoding and $(0\quad 0\quad \phi_r(\Gamma)/\sqrt{3}\quad \Gamma)^T$ for Hadamard encoding. These points were chosen to demonstrate the touching of the inscribing sphere and the dynamic range region. Typical values for Γ lie between 0% and 10%, depending on the sequence design. A short discussion for both SE- and GRE-based sequences is presented in Section 4.4 as well as in the Discussion section.

There are two regions of interest in which encoding can be operated. Encoding is 'dynamic range limited (DynR)' if the gradient strength is tuned such that the largest expected displacement is just within the dynamic range in-sphere of the applied encoding scheme. If the maximal gradient strength and encoding efficiency are chosen, but no expected displacement reaches or exceeds the dynamic range, encoding is 'gradient strength limited (Grad)'. In fractional, GRE-MRE sequences, the encoding efficiency is typically too low to reach the dynamic range limit, and hence acquisition is gradient strength limited. In contrast, SE-based sequences with long TEs usually can employ full-wave encoding with multiple sensitization cycles to maximize the accumulated phase. These acquisitions reach or even exceed the dynamic range limit.

2.1.3 | Displacement-to-noise ratio (DNR)

In order to quantify noise, the maximal DNR can be calculated from Equations 7 and 9 under the assumption that the full dynamic range ϕ_r is encoded. In this case, the DNR in all encoding directions is given by

$$\mathrm{DNR}_i^{\mathrm{DynR}} = \frac{r_{0,i}}{\sigma_{r,i}} = \frac{\sqrt{N_P}\phi_r}{2\sqrt{\left(\widehat{D}\widehat{D}^T\right)_{ii}}}\mathrm{SNR}. \tag{16}$$

TABLE 1 Comparison of phase contrast encoding schemes regarding key properties. Dynamic range region visualization: blue lines denote main coordinate axes, red lines denote directions of minimal dynamic range (green if they coincide with main axes) and black lines denote directions of maximal dynamic range (orange if they coincide with main axes)

Name	Encoding matrix $\widehat{E}$	Decoding matrix $\widehat{D}$	N_{Enc}	Gradient strength	Encoding directions	Disp. variance $\sigma_\phi^2/\sigma_\eta^2$	Disp. covariance $\mathrm{cov}_\phi/\sigma_\eta^2$	Encoding efficiency DynR	Encoding efficiency Grad	Visualization of dynamic range region	Dynamic range radii
Six-point REF.: 3,10,11,13,18,20,21,31,34	$\begin{bmatrix} +1 & 0 & 0 & +1 \\ -1 & 0 & 0 & +1 \\ 0 & +1 & 0 & +1 \\ 0 & -1 & 0 & +1 \\ 0 & 0 & +1 & +1 \\ 0 & 0 & -1 & +1 \end{bmatrix}$	$\frac{1}{2}\begin{bmatrix} +1 & -1 & 0 & 0 & 0 & 0 \\ 0 & 0 & +1 & -1 & 0 & 0 \\ 0 & 0 & 0 & 0 & +1 & -1 \\ \frac{1}{3} & \frac{1}{3} & \frac{1}{3} & \frac{1}{3} & \frac{1}{3} & \frac{1}{3} \end{bmatrix}$	6	1	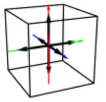	$\frac{1}{2}$	0	$\sqrt{\frac{8}{3}}$	$\sqrt{\frac{8}{3}}$	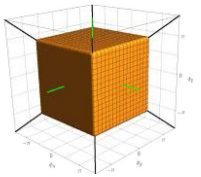	$\phi_r = \pi$ $\phi_R = \sqrt{3}\pi$
Six-point+ (maximal orthogonal encoding)	$\frac{1}{2}\begin{bmatrix} -1 & +2 & -2 & +2 \\ +1 & -2 & +2 & +2 \\ +2 & -1 & -2 & +2 \\ -2 & +1 & +2 & +2 \\ +2 & +2 & +1 & +2 \\ -2 & -2 & -1 & +2 \end{bmatrix}$	$\frac{1}{9}\begin{bmatrix} -1 & +1 & +2 & -2 & +2 & -2 \\ +2 & -2 & -1 & +1 & +2 & -2 \\ -2 & +2 & -2 & +2 & +1 & -1 \\ +\frac{3}{2} & +\frac{3}{2} & +\frac{3}{2} & +\frac{3}{2} & +\frac{3}{2} & +\frac{3}{2} \end{bmatrix}$	6	1.5	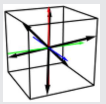	$\frac{2}{9}$	0	$\sqrt{\frac{8}{3}}$	$\sqrt{6}$	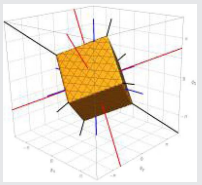	$\phi_r = 2\pi/3$ $\phi_R = 2\pi/\sqrt{3}$
Unbalanced four-point REF.: 12,17-19	$\begin{bmatrix} +1 & 0 & 0 & +1 \\ 0 & +1 & 0 & +1 \\ 0 & 0 & +1 & +1 \\ 0 & 0 & 0 & +1 \end{bmatrix}$	$\begin{bmatrix} +1 & 0 & 0 & -1 \\ 0 & +1 & 0 & -1 \\ 0 & 0 & +1 & -1 \\ 0 & 0 & 0 & +1 \end{bmatrix}$	4	1	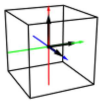	2	1	1	1	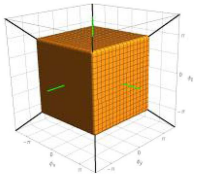	$\phi_r = \pi$ $\phi_R = \sqrt{3}\pi$
Unbalanced four-point+(maximal orthogonal encoding)	$\frac{1}{2}\begin{bmatrix} -1 & +2 & -2 & +2 \\ +2 & -1 & -2 & +2 \\ +2 & +2 & +1 & +2 \\ 0 & 0 & 0 & +2 \end{bmatrix}$	$\frac{1}{9}\begin{bmatrix} -2 & +4 & +4 & -6 \\ +4 & -2 & +4 & -6 \\ -4 & -4 & +2 & +6 \\ 0 & 0 & 0 & +9 \end{bmatrix}$	4	1.5	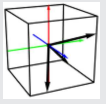	$\frac{8}{9}$	$\frac{4}{9}$	1	$\sqrt{\frac{9}{4}}$	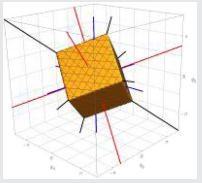	$\phi_r = 2\pi/3$ $\phi_R = 2\pi/\sqrt{3}$
Balanced four-point (tetrahedral encoding) REF.: 22	$\begin{bmatrix} -1 & +1 & +1 & +1 \\ +1 & -1 & +1 & +1 \\ +1 & +1 & -1 & +1 \\ +1 & +1 & +1 & +1 \end{bmatrix}$	$\frac{1}{2}\begin{bmatrix} -1 & 0 & 0 & +1 \\ 0 & -1 & 0 & +1 \\ 0 & 0 & -1 & +1 \\ +1 & +1 & +1 & -1 \end{bmatrix}$	4	$\sqrt{3}$	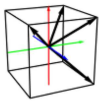	$\frac{1}{2}$	$\frac{1}{4}$	$\sqrt{\frac{4}{3}}$	$\sqrt{4}$	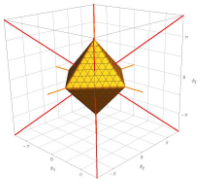	$\phi_r = \pi/\sqrt{3}$ $\phi_R = \pi$
Hadamard	$\begin{bmatrix} +1 & +1 & +1 & +1 \\ +1 & -1 & -1 & +1 \\ -1 & +1 & -1 & +1 \\ -1 & -1 & +1 & +1 \end{bmatrix}$	$\frac{1}{4}\begin{bmatrix} +1 & +1 & -1 & -1 \\ +1 & -1 & +1 & -1 \\ +1 & -1 & -1 & +1 \\ +1 & +1 & +1 & +1 \end{bmatrix}$	4	$\sqrt{3}$	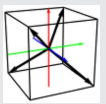	$\frac{1}{4}$	0	$\sqrt{\frac{8}{3}}$	$\sqrt{8}$	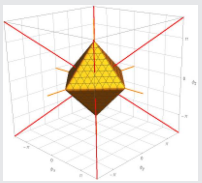	$\phi_r = \pi/\sqrt{3}$ $\phi_R = \pi$

In the gradient strength-limited regime, DNR is always lower and is given by

$$\mathrm{DNR}_i^{\mathrm{Grad}}(G) = \frac{\sqrt{N_\mathrm{P}}\left|r_{0,i}\right|\epsilon_f G}{2\sqrt{\left(\widehat{D}\widehat{D}^\mathrm{T}\right)_{ii}}}\mathrm{SNR} < \mathrm{DNR}_i^{\mathrm{DynR}}. \tag{17}$$

To estimate the DNR of an MRE acquisition, the local noise $\sigma_{r,i}\left(\vec{x}\right)$ in each of the three encoding axes *i*(*XYZ*) can be estimated from the standard error of the fit.[35] The DNR is then given by

$$\mathrm{DNR}_i\left(\vec{x}\right) = \frac{\left|r_i\left(\vec{x}\right)\right|}{\sigma_{r_i}\left(\vec{x}\right)} = \sqrt{\frac{N_\mathrm{P}}{2}}\frac{\left|\mathcal{F}_1^k\phi_{k,i}\left(\vec{x}\right)\right|}{\sqrt{\frac{1}{N_\mathrm{P}-1}\sum_{m=1}^{N_\mathrm{P}}\left(\phi_{m,i}\left(\vec{x}\right)-\frac{1}{2}\sum_{n\in\{1,N_\mathrm{P}-1,N_\mathrm{P}\}}\mathrm{e}^{\mathrm{i}2\pi nm/N_\mathrm{P}}\mathcal{F}_n^k\phi_{k,i}\left(\vec{x}\right)\right)^2}}, \tag{18}$$

where $\mathcal{F}$ denotes the DFT of the form $\mathcal{F}_m^n x_n = \frac{2}{N_\mathrm{P}}\sum_{n=1}^{N_\mathrm{P}} x_n \mathrm{e}^{-\mathrm{i}2\pi nm/N_\mathrm{P}}$.

2.1.4 | Encoding efficiency

The encoding efficiency of a scheme can be measured in terms of its achieved DNR divided by the root of encoding directions $\sqrt{N_\mathrm{Enc}}$. We present these in units of the encoding efficiency of the unbalanced four-point encoding scheme. In this way, the quantity reflects the relative increase in DNR efficiency, which could equally be achieved by sequential averaging of unbalanced four-point acquisitions

$$\zeta^{\mathrm{DynR}} = \frac{\mathrm{DNR}^{\mathrm{DynR}}}{\mathrm{DNR}^{\mathrm{DynR}}_{\mathrm{Unb.Four}}}\sqrt{\frac{4}{N_\mathrm{Enc}}} = \frac{\sqrt{8}\phi_r}{\sqrt{N_\mathrm{Enc}\left(\widehat{D}\widehat{D}^\mathrm{T}\right)_{ii}}\pi}. \tag{19}$$

In the gradient strength-limited regime, we assume that the gradient strength per channel and the encoding efficiency are held constant. Using Equation 17, the encoding efficiency is given by

$$\zeta^{\mathrm{Grad}} = \frac{\mathrm{DNR}^{\mathrm{Grad}}}{\mathrm{DNR}^{\mathrm{Grad}}_{\mathrm{Unb.Four}}}\sqrt{\frac{4}{N_\mathrm{Enc}}} = \frac{\sqrt{8}}{\sqrt{N_\mathrm{Enc}\left(\widehat{D}\widehat{D}^\mathrm{T}\right)_{ii}}}. \tag{20}$$

2.1.5 | Intra-voxel phase dispersion (IVPD)

In MRE, the shear displacement across a voxel is assumed to be constant. However, the displacement is a continuous function in space and hence application of a MEG leads to IVPD. This, in turn, can be shown to lead to magnitude fluctuations, which depend on the voxel size, the shear wavelength and the sensitizing gradient.[36,37] The ratio of the magnitude image with and without IVPD can be calculated by solving the integral

$$R_{i,k}\left(\vec{x}_c\right) = \left|\frac{1}{V}\int_{\Omega_V}\mathrm{d}^3x\,\mathrm{e}^{\mathrm{i}\varphi_{i,k}\left(\vec{x}+\vec{x}_c\right)}\right|. \tag{21}$$

As we are only interested in the effect of the encoding scheme on the magnitude of the IVPD signal, we assume a plane wave with wave number *k* to propagate in the *x*-direction and approximate its displacement in a Taylor series about the center of the voxel with extent Δx, which is valid in the regime $k\Delta x \ll 1$

$$\vec{r}\,(x,t) = \vec{r}_0\sin(kx+\theta) = \vec{r}_0\sin(\theta) + \vec{r}_0\cos(\theta)kx + O\left(x^2\right). \tag{22}$$

The IVPD-induced signal drop is then given by

$$R = \left|\mathrm{sinc}\left(k\frac{\Delta x}{2}\left(\vec{r}_0\cdot\vec{d}\right)G\epsilon_f\cos\left(\tilde{\theta}\right)\right)\right| \overset{*}{\geq} \left|\mathrm{sinc}\left(k\frac{\Delta x}{2}G\epsilon_f\left\|\vec{r}_0\right\|_2\left\|\vec{d}\right\|_2\right)\right|, \tag{23}$$

where we use the fact that the unnormalized sinc-function, sinc(*x*) = $\sin(x)x^{-1}$, is a monotonically decreasing function in the interval $(0,\pi)$, $k\Delta x \ll 1$ as well as $G\left\|\vec{r}_0\right\|_2\left\|\vec{d}\right\|_2\epsilon_f \leq \pi$, i.e. we encode motion without phase wrapping. As sinc($x \ll 1$) ≈ $1 - x^2/6$, IVPD-based signal loss increases with the square of the total gradient strength $G\left\|\vec{d}\right\|_2$, encoding efficiency and displacement amplitude, and is inherently coupled to the ratio of resolution and shear wavelength.[36] Hence, encoding schemes with higher total gradient strength can suffer from increased IVPD, which, in turn, leads to decreased DNR. This is of particular importance for very soft materials with small wavelengths and coarse resolution.

2.2 | Effects of readout and phase-encoding gradient

Referring to Figure 1, both readout and phase-encoding gradients lead to a gradient of the phase, which is superimposed on the image encoding. These gradients of the phase are dependent on the readout and phase encoding gradient strength, as well as the local shear wave displacement. Solving Equation 2 for periodic motion in the presence of a constant readout gradient, the temporal phase dependence in the time interval $\mathrm{TE}-{}^{1}/_{2\mathrm{BW}} \leq t \leq \mathrm{TE}+{}^{1}/_{2\mathrm{BW}}$ (BW, readout bandwidth) is given by

$$\phi(t) = \frac{\gamma \vec{G}\cdot\vec{r}_0(\vec{x})}{2\pi f}\left[\cos\left(2\pi f\left(\mathrm{TE}-\frac{1}{2\mathrm{BW}}\right)+\theta(\vec{x})+\frac{2\pi k}{N_\mathrm{P}}\right)-\cos\left(2\pi f t+\theta(\vec{x})+\frac{2\pi k}{N_\mathrm{P}}\right)\right]. \tag{24}$$

In the limit of the readout bandwidth being much larger than the underlying frequency of the shear wave, i.e. $BW \gg f$, the phase can be linearized to

$$\phi(t) \approx const + \underbrace{\gamma \vec{G}(t-\mathrm{TE})}_{=\vec{k}} \cdot \vec{r}_0(\vec{x})\sin\left(2\pi f \mathrm{TE}+\theta(\vec{x})+2\pi N_\mathrm{P}^{-1}k\right)+O\left((t-\mathrm{TE})^2\right), \tag{25}$$

where $\gamma \vec{G}(t-\mathrm{TE}) = \vec{k}$ is the k vector of the readout or phase encoding direction. The time constant contribution can be treated as part of the spurious imaging gradient phase contribution. Application of the Fourier shift theorem to the first-order term reveals that the gradient of the phase causes a local shift of the image proportional to $\vec{r}_0 \cdot \vec{G} / \left\| \vec{G} \right\|_2$. As typical displacements are on the order of 1–100 μm, the local distortions are much smaller than the actual resolution of MRE scans (2–4 mm) and can be neglected.

3 | METHODS

MRE data were collected on a gel phantom with four circular inclusions (CIRS Inc., Norfolk, VA, USA) using the six encoding schemes (Table 1) implemented on a 3-T Philips Ingenia system (Philips Healthcare, Best, the Netherlands). Signal was received using a 15-channel head coil and a 100 Hz electro-magnetic actuation was employed. Seven repeat measurements were acquired for each scheme to calculate DNR, as well as to assess the accuracy and precision of reconstructed stiffness maps. All measurements were performed using a GRE-based fractional MRE sequence,[30] with 180 Hz, 12 mT/m bipolar MEGs, eight phase offsets, 14 slices, 2 mm isotropic resolution, 0.2 mm slice gap and 112 × 80 matrix size acquired using a 20° flip angle, Cartesian readout and sensitivity encoding (SENSE)[38] with two-fold acceleration. Encoding was performed in the gradient strength-limited regime. The acquisition of a full volumetric set of eight mechanical phase offset images took 45 s per encoding direction. Synchronization to the external wave generator was achieved using a transistor-transistor logic (TTL) trigger signal and the repetition time (TR) was set equal to the wave period of 10 ms.

In vivo data of the liver were acquired using the unbalanced four-point and Hadamard encoding schemes in one healthy volunteer on informed consent and according to institutional guidelines. Experiments were performed on a 3-T Philips Achieva system using a six-channel cardiac coil, 60 Hz electro-mechanical actuation and the GRE-based fractional MRE sequence,[30] with 156 Hz, 19.8 mT/m bipolar MEGs, 4 mm isotropic resolution, no slice gap and 10 slices filling a matrix of 80 × 52, with SENSE acceleration of 2 and four breath holds of 19 s each. Eight phase offsets were acquired for both encoding schemes and the experiment was repeated twice for comparability.

Data post-processing included phase unwrapping along the mechanical phase dimension, subtraction of the mean phase to remove field inhomogeneity effects, decoding and subsequent Fourier transformation along the mechanical phase dimension. The peak corresponding to the actuation frequency was evaluated and divided by the encoding efficiency of the respective MEGs to obtain complex displacement values in units of micrometers. These were then masked using the magnitude images and a hand-drawn region of interest (ROI), which was copied onto all scans. The shear wave velocity (phantom) and the magnitude of the complex shear modulus (*in vivo*) were reconstructed from the masked displacement data by local inversion of the viscoelastic complex wave equation.[35] The curl operator was applied prior to inversion to filter out compressional wave components. In addition, the displacement fields in the *in vivo* acquisitions were Gaussian filtered prior to inversion for smoother spatial derivatives.

4 | RESULTS

4.1 | Comparison of encoding schemes

In Table 1, the results of the theoretical evaluation of the six encoding schemes are presented.

4.1.1 | Dynamic range

The dynamic range of unbalanced four-point and six-point encoding is given by π. Increasing the overall gradient strength by employing overplus encoding decreases the dynamic range to $2\pi/3$ in accordance with the 1.5-fold increase in total gradient strength. Both balanced and Hadamard

encoding share the lowest dynamic range with $\pi/\sqrt{3}$, which is approximately 1.77 times lower than unbalanced four-point encoding. In addition, the dynamic range regions of balanced and Hadamard encoding are not cubic, and hence phase wraps may amount to non-integer multiples of π once the dynamic range limit is exceeded.[23]

4.1.2 | Noise variance and correlation

The unbalanced four-point encoding scheme shows the highest noise variance, whereas the six-point overplus technique shows the lowest. Balanced and six-point encoding both show four-fold lower noise variance than unbalanced four-point encoding; however, balanced encoding suffers from noise correlation between the displacement estimates. Hadamard encoding and six-point encoding are capable of estimating the displacements with independent noise statistics.

4.2 | Dynamic range limit

In the dynamic range limit, we assume that the gradient strength of the overplus technique is reduced by 1.5 in each gradient channel and by $\sqrt{3}$ for balanced and Hadamard encoding.

4.2.1 | Encoding efficiency

By definition, the encoding efficiency of unbalanced four-point encoding is one. Six-point encoding has an efficiency of $\sqrt{8/3}$, which is equivalent to approximately 2.6-fold averaging of unbalanced four-point encoding. The encoding efficiency of the regular and overplus techniques is equal as overplus is only a rotation and scaling of the gradient system, which is reversed in the dynamic range limit. Reduction of the gradient strength by $\sqrt{3}$ in the balanced four-point scheme leads to reduced encoding efficiency of $\sqrt{4/3}$, whereas Hadamard encoding has the same efficiency as six-point encoding.

It should be noted that the encoding efficiency takes the number of encoding directions and hence acquisition time into account. Hadamard encoding shows $\sqrt{2/3}$ lower DNR than an equally dynamic range-limited six-point acquisition, but only uses two-thirds of the acquisition time.

4.2.2 | IVPD

As the dynamic range was found to inversely scale with the total gradient strength for the analyzed schemes, IVPD will be equal for all employed schemes and will not affect the DNR comparison.

4.3 | Gradient strength limit

In the gradient strength limit, the dynamic range radii of all compared schemes are larger than the maximally expected displacement.

4.3.1 | Encoding efficiency

The encoding efficiency of the unbalanced four-point scheme is one. As the gradient strength per channel is limited, overplus unbalanced four-point encoding increases the overall gradient strength and leads to 1.5 times larger encoding efficiency, which is equivalent to 2.25-fold averaging. Balanced encoding shows an increase by $\sqrt{4}$ in DNR, whereas Hadamard encoding leads to a $\sqrt{8}$-fold increase. Six-point encoding has higher encoding efficiency than overplus unbalanced four-point encoding, but lower than balanced encoding, whereas its overplus variant falls short of Hadamard encoding with an efficiency of $\sqrt{6}$. Again, it should be noted that the overall DNR performance of overplus six-point encoding is approximately 6% higher than Hadamard encoding, but at the cost of a 50% longer scan duration.

4.3.2 | IVPD

In the gradient strength limit, IVPD can adversely affect the DNR of high gradient strength schemes, as shown in Equation 23; however, it is highly dependent on resolution, local wavelength, displacement and encoding efficiency. If IVPD is present with unbalanced four-point or six-point encoding, overplus as well as balanced and Hadamard encoding will lead to increased IVPD-based signal drop.

4.4 | Comparison of full-wave and fractional encoding in SE- and GRE-MRE sequences

In order to set perspective on the two encoding limits, two references were selected to demonstrate the difference in encoding efficiencies between SE- and GRE-MRE sequences. Sack et al.[34] used an SE-MRE sequence with echo planar imaging (EPI) readout and full-wave encoding with two sinusoidal gradient lobes to encode vibrations in the brain of a volunteer. They reported a gradient strength of 35 mT/m, six-point encoding and 50 Hz vibrations. The encoding efficiency can be determined by solving Equation 4.[30] Here, the encoding efficiency is 5.28 rad/mm/(mT/m). Hence, reported displacements of 50 μm lead to a maximal accumulated phase of 9.23 rad, which is above the dynamic range of six-point encoding when no phase unwrapping is taken into account. With unwrapping of a single wrap, the dynamic range is extended to 3π and the acquisition lies just within the dynamic range.

Garteiser et al.,[12] in contrast, proposed a GRE-based fractional encoding sequence in which multiple phase images were acquired per wave cycle. They reported 160-Hz MEGs, unbalanced four-point encoding and otherwise similar parameters to those of Sack et al.[34] For comparability, we assume the same 50-Hz vibrations, 35 mT/m and sinusoidal gradient shape. The encoding efficiency is 0.48 rad/mm/(mT/m), which leads to an accumulated phase of 0.85 rad, well below the dynamic range of unbalanced four-point encoding. Hence, encoding is performed in the gradient strength-limited regime.

The imaging gradient to MEG encoding efficiency ratio Γ depends on the exact imaging gradient strength, timing and duration. For the above GRE-MRE sequence, Γ can be estimated to be approximately 6%, assuming typical multishot GRE-MRE sequence parameters. Depending on the exact sequence timing of the aforementioned SE-MRE sequence, which is not known to the authors, Γ can be expected to be in the range of 0–5%.

4.5 | Phantom data

In Figure 3, magnitude images of one selected slice, encoding direction and phase offset, together with the corresponding real part of the complex displacement, as well as reconstructed shear wave velocities, are shown for all six encoding schemes. The displacement maps are in very good quantitative and qualitative agreement, where enhanced noise is clearly visible in unbalanced four-point encoding and its overplus variant when compared with the other schemes. The increased noise in the unbalanced four-point acquisitions leads to pronounced noise in reconstructed shear wave velocities.

In Figure 4, correlation plots for all six encoding schemes compared with the unbalanced four-point scheme are shown. Here, the magnitude of each displacement component was compared pixel-wise between the schemes, showing excellent correlation. Increased DNR is visible in the higher packing of individual observations (dots) in the six-point, balanced four-point and Hadamard encoding schemes (bottom row and top left).

In Figure 5, DNR according to Equation 18 is shown as the volumetric and directional average of each experiment (black dots), as well as its ensemble average (black bar). The red triangles denote the theoretical values according to Equation 17, where the underlying magnitude SNR was fitted to best represent the ensemble averages. Unbalanced four-point encoding shows an average DNR of 18.9 ± 0.5, compared with Hadamard encoding with 49.2 ± 1.8, balanced encoding with 35.6 ± 0.8 and overplus six-point encoding with 51.2 ± 1.0. This corresponds well to the theoretical DNR increase of $\sqrt{8}$ for Hadamard, 2 for balanced and 3 for overplus six-point encoding, respectively.

In Figure 6, ROI-averaged isotropic shear wave velocities are reported for the six encoding schemes. Five ROIs were defined to measure the average velocity in the four inclusions as well as the background gel. Soft regions (inclusions 3 and 4) are all equally well reconstructed, yielding averaged shear wave velocities of 1.328 ± 0.002 and 1.147 ± 0.006 m/s over all encoding schemes. The background (1.636 ± 0.005 m/s) and

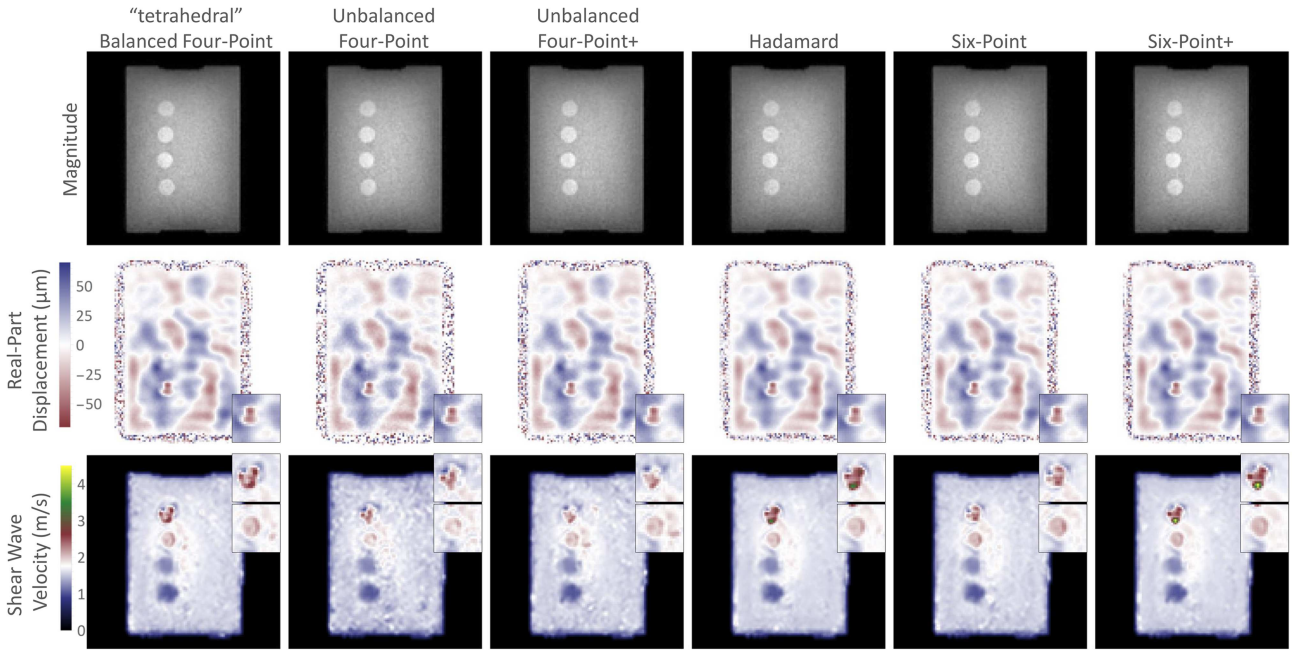

FIGURE 3 Comparison of magnitude images, real part of shear displacements and magnitude of shear wave velocities of the six encoding schemes for one slice, and one experiment (no averaging). Magnitude images have equal signal-to-noise ratio (SNR) per encoding direction and do not show variations as a result of intra-voxel phase dispersion. Increased noise of unbalanced four-point encoding in comparison with Hadamard and six-point encoding is clearly visible in the displacement maps. The small inset is a zoom of the region around the softest inclusion. The shear wave velocity maps are all in very good visual agreement; however, the decreased displacement-to-noise ratio (DNR) of the unbalanced four-point schemes leads to increased noise compared with balanced, Hadamard and six-point encoding, as well as an underestimation of the stiffness of the two stiffest inclusions (insets)

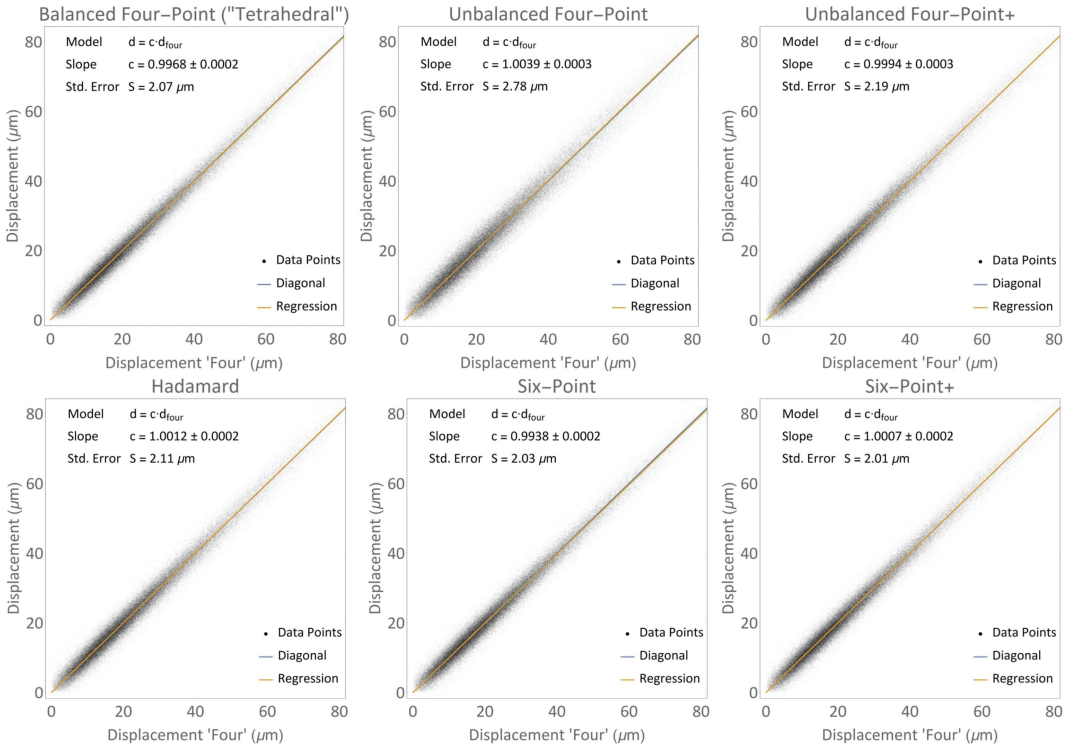

FIGURE 4 Correlation plots showing the displacement correlation of unbalanced four-point encoding and all other five encoding schemes. Correlation was calculated per voxel for the magnitude of each complex component of the displacement field. Linear regression shows very high correlation of unbalanced four-point encoding and all other schemes, showing that all schemes captured the displacement field equally (Std. Error, standard error of the estimate). Increased standard error of the estimate for the unbalanced four-point scheme suggests increased displacement noise compared with the other schemes. However, it should be noted that two different experiments are compared, so that experimental influences, such as actuator drift, influence the correlation

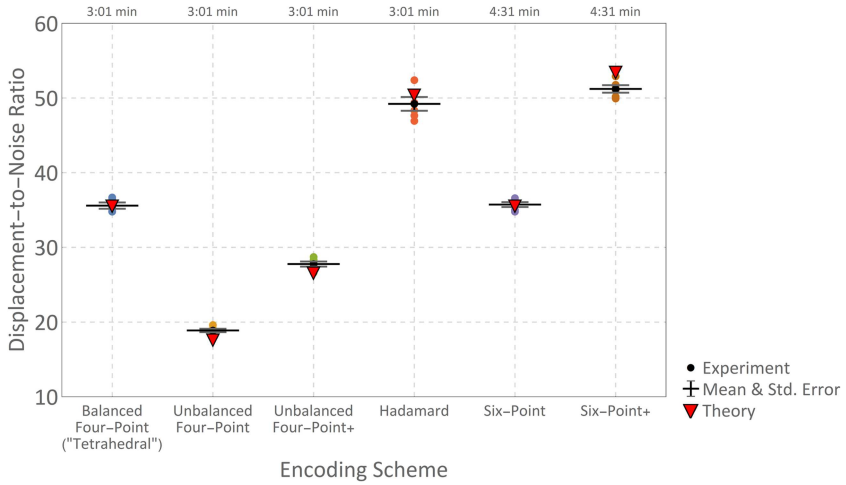

FIGURE 5 Displacement-to-noise ratio (DNR) comparison of the six encoding schemes calculated from seven consecutively repeated magnetic resonance elastography (MRE) experiments each (points). The centered black bars denote the ensemble mean and the gray error bars are the standard deviations of averaged DNRs over all measurements. The red triangles denote the theoretical DNR, whose underlying signal-to-noise ratio (SNR) was fitted to best fit the ensemble average of the DNR for all encoding schemes. The total scan duration for each encoding direction is denoted above the figure

inclusion 2 (1.915 ± 0.008 m/s) are also well captured with all schemes; however, unbalanced four-point encoding underestimates the stiffness compared with the other schemes by 1% (background) and 10% (inclusion 2). The stiffest inclusion shows very high variability within and between encoding schemes as a result of the wavelength being longer than the extent of the object. Unbalanced four-point encoding shows severe underestimation of the stiffness, leading to inverted ordering of inclusions 1 and 2. With increasing encoding efficiency, the shear wave velocity of the inclusion increases and shows lower intra-scheme standard deviation. Schemes with similar DNR (Figure 5) also show similar reconstructed stiffness values. This finding suggests that high DNR is especially crucial for the reliable recovery of high stiffness regions.

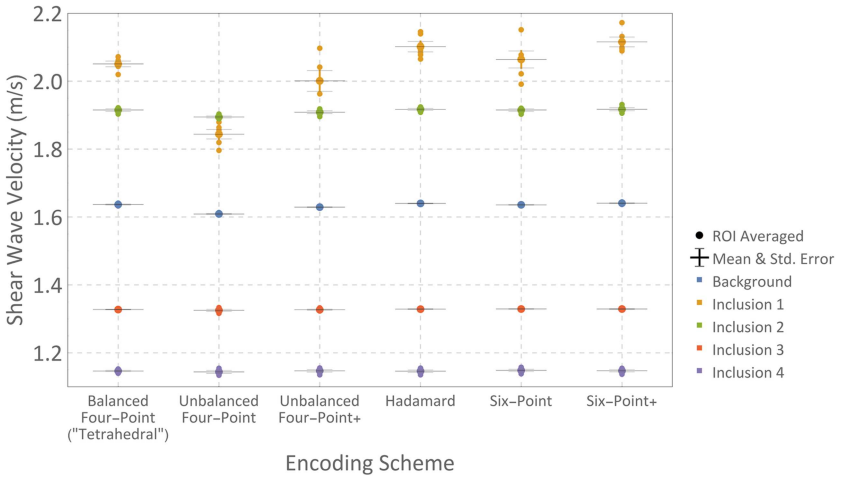

FIGURE 6 Comparison of region of interest (ROI)-averaged isotropic shear wave velocity of all six encoding schemes and seven experiment repetitions (points). ROIs were defined to select spherical inclusions (1–4) as well as the surrounding background. Reconstruction of the shear wave velocity was performed using the local isotropy assumption, curl filtering and local inversion of the complex viscoelastic wave equation without spatial Gaussian filtering.[35] In low-velocity regions of <1.7 m/s (background, inclusions 3 and 4), the shear wavelength is smaller than the extent of the inclusions and velocity reconstruction can be performed reliably. In high-velocity regions, where wavelengths are comparable or larger than the inclusions, wave inversion is only possible with sufficient displacement-to-noise ratio (DNR) (six+ and Hadamard). Unbalanced four-point encoding severely underestimates the stiffness of inclusion 1

4.6 | *In vivo* data

In Figure 7, the comparison of unbalanced four-point and Hadamard encoding of the liver of one healthy volunteer is shown. Magnitude images as well as the real part of the complex displacement in the slice direction and the magnitude of the masked complex shear stiffness are presented.

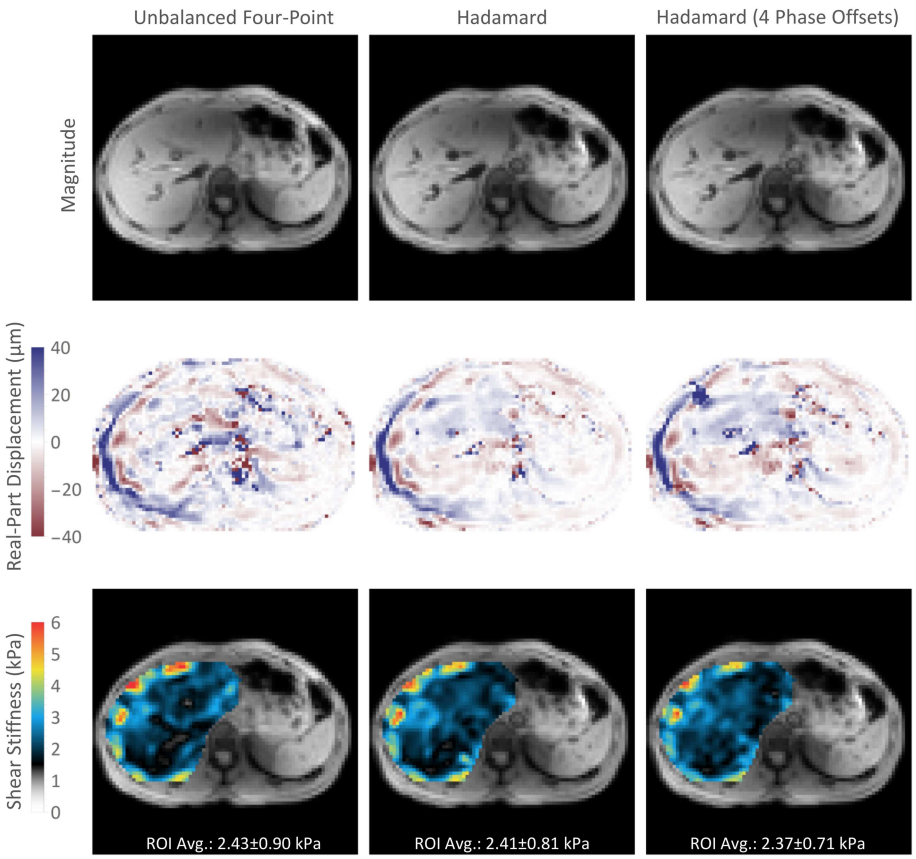

FIGURE 7 Comparison of magnitude images, real part of shear displacements (cropped to ±40 µm) and magnitude of shear stiffness maps of unbalanced four-point (left) and Hadamard (center) encoded magnetic resonance elastography (MRE) of the liver in one healthy volunteer, as well as a retrospectively reduced Hadamard scan with four phase offsets instead of eight (right). All scans were performed in four breath-holds of 19 s. Region of interest (ROI)-averaged liver stiffnesses are in very good agreement for all three scans

Both magnitude images are in very good agreement showing similar SNR and anatomy. It should be noted that blood vessels are darker in the Hadamard scan than in the unbalanced four-point encoding, which can be attributed to the larger first gradient moment and subsequently higher signal loss through IVPD originating from blood flow. The displacement maps are in good agreement; however, changes in wave coupling between the experiments as well as different breath hold positions influence the displacement field. Reconstruction of the shear stiffness magnitudes shows very good agreement between the scans. The ROI-averaged stiffness magnitude in the displayed slice was 2.43 ± 0.90 kPa (2.47 ± 0.83 kPa) for unbalanced four-point encoding and 2.41 ± 0.81 kPa (2.43 ± 0.83 kPa) for Hadamard encoding. The values in parentheses denote the respective values of the repeat experiments.

The gain in DNR with Hadamard encoding can be traded with reduced scan time by acquiring four instead of eight mechanical phase offsets. This reduces the total scan duration from four to two breath holds. We retrospectively reduced the number of acquired mechanical phases and reconstructed the complex displacement vector as well as the shear stiffness. The results are shown in the third column of Figure 7. Reconstructed displacement fields and shear stiffness maps are in very good agreement. The ROI-averaged stiffness was 2.37 ± 0.71 kPa (2.40 ± 0.76 kPa).

5 | DISCUSSION

A theoretical framework to evaluate MRE motion encoding schemes with respect to achievable DNR and dynamic range has been formulated, together with a metric of encoding efficiency relating DNR and acquisition time. We have shown that motion sensitization can be performed according to two fundamental limits: the dynamic range- and gradient strength-limited regimes.

The theoretical DNR predictions have been validated in a comprehensive phantom study using a GRE-based fractional MRE sequence, which was operated in the gradient strength-limited regime. We found excellent correlation of the displacement fields for all six encoding schemes when compared with the unbalanced four-point scheme, which is considered to be the gold standard in GRE-MRE. The calculated DNRs from the spectral representation of the mechanical phase offsets (Equation 18) were found to correspond well with theoretical predictions of Equation 17.

The reconstructed shear wave velocities were in very good quantitative agreement for all six schemes in the soft regime (<1.7 m/s). In high stiffness regions, the low DNR of unbalanced four-point encoding led to underestimation of the shear wave velocity. For the stiffest inclusions, encoding schemes with similar DNR also recovered similar velocity values. As displacements were found to be well correlated between all schemes, the increase in DNR between the different encoding schemes directly leads to enhanced wave inversion performance. This is crucial, for instance, in the oncology domain, where lesions are often stiffer than the surrounding tissue habitat. The present analysis hence serves to enhance the impact of MRE for providing diagnostically useful data in the clinical arena.

In practice, DNR is often increased by averaging multiple measurements or by increasing temporal resolution within one wave cycle.[12,15,16] Theoretical predictions and results from the phantom demonstrated that, in the gradient strength-limited regime, high DNR schemes, such as Hadamard and overplus six-point encoding, can increase DNR by $\sqrt{8}$ and $\sqrt{9}$, respectively, which is equivalent to eight- and nine-fold averaging without an increase in the total scan duration. In the dynamic range limit, however, the increase is limited to $\sqrt{8/3}$ for both schemes because of the reduced applicable gradient strength.

A framework similar to ours was developed by Nir et al.[24] for the optimization-based design of MRE sequences. In their work, the encoding equation was posed to directly solve for the in- and out-of-phase components of the displacement field and to define an acquisition design matrix (here the encoding matrix) that transfers the displacement components into the measured motion phases. In the present work, we were interested in optimizing motion encoding for conventional MRE, which is based on the sequential acquisition of multiple phase offsets for each encoding direction and subsequent Fourier transformation to obtain displacements. The acquisition design matrix as defined by Nir et al.[24] for such an experiment would implicitly contain the DFT for each encoding direction. By solving for the real motion phases $\vec{\phi}_k\left(\vec{x}\right)$ instead of the complex displacements, the encoding matrix can be simplified stating only the real gradient directions. The Fourier transformation is then applied on the decoded motion phases. Central to our proposed framework is the inclusion of imaging gradients into the formalism, allowing correction for their spurious contribution $\delta_k\left(\vec{x}\right)$. Such a term is missing in the work of Nir et al.,[24] limiting the framework to specifically designed SE-MRE sequences that allow the nulling or strong reduction of the influence of imaging gradients.

Among the four analyzed encoding schemes utilizing the minimum number of four encoding directions, Hadamard encoding was shown to be the most effective. The Ansatz of D-optimal design[39] used in the framework by Nir et al.,[24] can be transferred to our formalism. The elements of the encoding matrix are constrained to be of magnitude less or equal to one, so as not to exceed the maximum gradient strength per axis. Hence, the problem of finding the D-optimal encoding matrix $\widehat{E}$ that maximizes $\left|\det\left(\widehat{E}^{\mathrm{T}}\widehat{E}\right)\right|$ is Hadamard's maximum determinant problem.[40] Thus, under the assumption of D-optimality, Hadamard encoding is the optimal encoding scheme when the minimal number of four encoding directions is used.

We note that the derivation of the covariance matrix assumes uncorrelated phase noise with zero mean and a finite standard deviation for all encoding directions. Although a finite standard deviation is generally given and often assumed in phase noise considerations,[24,30,41,42] e.g. changes in gradient temperature, wave actuation or induced mechanical vibrations may lead to systematic errors (non-zero mean) or an encoding direction- and phase offset-dependent standard deviation as well as correlated noise. Although the discussion of systematic errors is beyond the scope of this article, changes in standard deviation, as well as correlations, can be considered in the derivation of the covariance matrix (Appendix A) by replacing

$E[\eta_k \eta_m] = \sigma_\eta^2 \delta_{km} \rightarrow \mathrm{cov}_{\eta,km}$ with the covariance matrix of the phase noise $\mathrm{cov}_{\eta,\,km}$. The generalized covariance matrix of the reconstructed motion phases is then given by $\mathrm{cov} = \hat{D}\,\mathrm{cov}_\eta \hat{D}^{\mathrm{T}}$.

In the present work, conclusions regarding the encoding efficiency of the proposed encoding schemes are based on the DNR metric. A strain-based SNR measure (OSS-SNR) has been proposed previously in the literature[43] as an alternative quality metric for MRE. However, OSS-SNR depends on numerical spatial derivatives and hence on processing parameters, such as the finite difference scheme used, interpolation and smoothing operations. In contrast, the DNR is parameter-free and can be directly evaluated using the phase data, provided that no higher harmonic waves are present. Hence, the DNR metric was chosen for its analytical ease-of-use and straightforward experimental comparability.

If the dynamic range is exceeded at the cost of possible phase wrapping, the encoding efficiency can be further increased. In the present analysis, we assumed that no phase unwrapping is applied prior to decoding. As multiple wave phase offsets per encoding direction are acquired, the unwrapping of at least one phase wrap is possible.[44-47] As the encoding schemes only measure different projections of the displacement field, phase wrapping and subsequent unwrapping of each encoding direction can be applied prior to decoding. Hence, unwrapping equally extends the dynamic range of all the present schemes ($\pi \rightarrow (2n + 1)\pi$ in Equations 11 and 15, with n being the number of unwrappable phase wraps), and the DNR comparison, as well as the two discussed limits, remain valid in the presence of phase wraps.

A key indicator for the need to correct for imaging gradient offsets is the ratio of the imaging gradient to the MEG encoding efficiency Γ. As only small adjustments to the gradient timing and strength are possible in GRE-MRE, Γ is primarily influenced by changes in the encoding efficiency of the MEGs. Accordingly, only minor adjustments are possible and values of Γ well above 1% are typical. In contrast, SE-MRE sequences permit greater gradient timing flexibility, thereby allowing the reduction in the influence of imaging gradients. For example, by playing out pre-winding and rewinding gradients over a full wave period or by using flow compensation, the impact of imaging gradients is reduced or nulled. Furthermore, the long TEs in SE-MRE permit the use of full-wave encoding with multiple MEG repetitions, leading to orders of magnitude larger MEG encoding efficiency when compared with GE-MRE. If carefully designed, SE-MRE sequences allow the reduction of Γ to values well below 1%. In this case, reference-less methods, including SLIM and MD-RME, are applicable.

In the present work, it has been shown that Hadamard encoding can be used in fractional GRE-MRE acquisitions of the liver. The increase in DNR can be used to accelerate the MRE acquisition by acquiring only four instead of eight wave phases, allowing for the acquisition of a full liver MRE of the whole three-dimensional displacement field in only two breath holds of 19 s each.

The gain in DNR with overplus and Hadamard encoding, relative to unbalanced four-point and six-point encoding, can also be used to decrease the gradient duty cycle by respective scaling of the gradients. This may allow for shorter TRs, increased gradient duration or higher slew rates. However, the gradient duty cycle may also cause limitations in the applicable maximal gradient strength necessitating the scaling of the applied MEGs. As no difference in gradient duty cycle should be expected for equal total gradient strength, the minimal encoding efficiency in the gradient strength limit is given by the dynamic range-limited values. Hence, fractional GRE-MRE should always benefit from switching from unbalanced four-point to Hadamard encoding.

Previous literature used balanced four-point encoding ('tetrahedral encoding') for their GRE-MRE acquisitions.[22] Balanced four-point encoding suffers from the same dynamic range, potential gradient duty cycle and IVPD limitations as Hadamard encoding. However, it comes with $\sqrt{2}$ lower DNR independent of the regime in which it is operated, and exhibits correlated noise in reconstructed displacement fields compared with uncorrelated noise in Hadamard encoding. Hence, Hadamard encoding should be preferred over tetrahedral encoding.

6 | CONCLUSIONS

In GRE-MRE, Hadamard encoding provides a significant increase in encoding efficiency relative to standard unbalanced four-point schemes, permitting a decrease in scan duration of MRE protocols by a factor of two.

ACKNOWLEDGEMENTS

This project received funding from the European Union's Horizon 2020 research and innovation programme under grant agreement No. 668039.

ORCID

Christian Guenthner http://orcid.org/0000-0001-8707-7016
Jurgen Henk Runge http://orcid.org/0000-0003-4190-3890
Sebastian Kozerke http://orcid.org/0000-0003-3725-8884

REFERENCES

1. Muthupillai R, Rossman PJ, Lomas DJ, Greenleaf JF, Riederer SJ, Ehman RL. Magnetic resonance imaging of transverse acoustic strain waves. *Magn Reson Med*. 1996;36(2):266-274.
2. McGrath DM, Ravikumar N, Beltrachini L, Wilkinson ID, Frangi AF, Taylor ZA. Evaluation of wave delivery methodology for brain MRE: insights from computational simulations. *Magn Reson Med*. 2017;78(1):341-356.
3. Anderson AT, Van Houten EEW, McGarry MDJ, et al. Observation of direction-dependent mechanical properties in the human brain with multi-excitation MR elastography. *J Mech Behav Biomed Mater*. 2016;59:538-546.

4. Fehlner A, Papazoglou S, McGarry MD, et al. Cerebral multifrequency MR elastography by remote excitation of intracranial shear waves. *NMR Biomed*. 2015;28(11):1426-1432.
5. Numano T, Mizuhara K, Hata J, Washio T, Homma K. A simple method for MR elastography: a gradient-echo type multi-echo sequence. *Magn Reson Imaging*. 2015;33(1):31-37.
6. Honarvar M, Rohling R, Salcudean SE. A comparison of direct and iterative finite element inversion techniques in dynamic elastography. *Phys Med Biol*. 2016;61(8):3026-3048.
7. Tzschätzsch H, Guo J, Dittmann F, Braun J, Sack I. Tomoelastography by multifrequency wave number recovery. In: Handels H, Ehrhardt J, Horsch A, Meinzer H-P, Tolxdorff T, eds. *Bildverarbeitung für die Medizin 2006*. Informatik aktuell. Berlin, Heidelberg: Springer Berlin Heidelberg; 2016:3-7.
8. Honarvar M, Lobo J, Mohareri O, Salcudean SE, Rohling R. Direct vibro-elastography FEM inversion in Cartesian and cylindrical coordinate systems without the local homogeneity assumption. *Phys Med Biol*. 2015;60(9):3847-3868.
9. Petrov AY, Docherty PD, Sellier M, Chase JG. Multi-frequency inversion in Rayleigh damped magnetic resonance elastography. *Biomed Signal Process Control*. 2014;13:270-281.
10. Johnson CL, McGarry MDJ, Van Houten EEW, et al. Magnetic resonance elastography of the brain using multishot spiral readouts with self-navigated motion correction. *Magn Reson Med*. 2013;70(2):404-412.
11. Johnson CL, Holtrop JL, McGarry MDJ, et al. 3D multislab, multishot acquisition for fast, whole-brain MR elastography with high signal-to-noise efficiency. *Magn Reson Med*. 2014;71(2):477-485.
12. Garteiser P, Sahebjavaher RS, Ter Beek LC, et al. Rapid acquisition of multifrequency, multislice and multidirectional MR elastography data with a fractionally encoded gradient echo sequence. *NMR Biomed*. 2013;26(10):1326-1335.
13. Yasar TK, Klatt D, Magin RL, Royston TJ. Selective spectral displacement projection for multifrequency MRE. *Phys Med Biol*. 2013;58(16):5771-5781.
14. Klatt D, Yasar TK, Royston TJ, Magin RL. Sample interval modulation for the simultaneous acquisition of displacement vector data in magnetic resonance elastography: theory and application. *Phys Med Biol*. 2013;58(24):8663-8675.
15. Klatt D, Johnson CL, Magin RL. Simultaneous, multidirectional acquisition of displacement fields in magnetic resonance elastography of the in vivo human brain. *J Magn Reson Imaging*. 2015;42(2):297-304.
16. Romano A, Scheel M, Hirsch S, Braun J, Sack I. In vivo waveguide elastography of white matter tracts in the human brain. *Magn Reson Med*. 2012;68(5):1410-1422.
17. Sinkus R, Lorenzen J, Schrader D, Lorenzen M, Dargatz M, Holz D. High-resolution tensor MR elastography for breast tumour detection. *Phys Med Biol*. 2000;45(6):1649-1664.
18. Sack I, Rump J, Elgeti T, Samani A, Braun J. MR elastography of the human heart: noninvasive assessment of myocardial elasticity changes by shear wave amplitude variations. *Magn Reson Med*. 2009;61(3):668-677.
19. Sahebjavaher RS, Frew S, Bylinskii A, et al. Prostate MR elastography with transperineal electromagnetic actuation and a fast fractionally encoded steady-state gradient echo sequence. *NMR Biomed*. 2014;27(7):784-794.
20. Maderwald S, Uffmann K, Galbán CJ, de Greiff A, Ladd ME. Accelerating MR elastography: a multiecho phase-contrast gradient-echo sequence. *J Magn Reson Imaging*. 2006;23(5):774-780.
21. Low G, Owen NE, Joubert I, et al. Reliability of magnetic resonance elastography using multislice two-dimensional spin-echo echo-planar imaging (SE-EPI) and three-dimensional inversion reconstruction for assessing renal stiffness. *J Magn Reson Imaging*. 2015;42(3):844-850.
22. Oliphant TE, Manduca A, Ehman RL, Greenleaf JF. Complex-valued stiffness reconstruction for magnetic resonance elastography by algebraic inversion of the differential equation. *Magn Reson Med*. 2001;45:299-310.
23. Pelc NJ, Bernstein MA, Shimakawa A, Glover GH. Encoding strategies for three-direction phase-contrast MR imaging of flow. *J Magn Reson Imaging*. 1991;1(4):405-413.
24. Nir G, Sahebjavaher RS, Sinkus R, Salcudean SE. A framework for optimization-based design of motion encoding in magnetic resonance elastography. *Magn Reson Med*. 2015;73(4):1514-1525.
25. Souza SP, Szumowski J, Dumoulin CL, Plewes DP, Glover GH. SIMA: simultaneous multislice acquisition of MR images by Hadamard-encoded excitation. *J Comput Assist Tomogr*. 1988;12(6):1026-1030.
26. Dumoulin CL, Souza SP, Darrow RD, Pelc NJ, Adams WJ, Ash SA. Simultaneous acquisition of phase-contrast angiograms and stationary-tissue images with Hadamard encoding of flow-induced phase shifts. *J Magn Reson Imaging*. 1991;1(4):399-404.
27. Guenthner C, Runge JH, Sinkus R, Kozerke S. Hadamard encoding for magnetic resonance elastography. *Proceedings of the 25th Annual Meeting ISMRM*, Honolulu, HI, 2017:1378.
28. Moran PR. A flow velocity zeugmatographic interlace for NMR imaging in humans. *Magn Reson Imaging*. 1982;1(4):197-203.
29. Muthupillai R, Ehman RL. Magnetic resonance elastography. *Nat Med*. 1996;2(5):601-603.
30. Rump J, Klatt D, Braun J, Warmuth C, Sack I. Fractional encoding of harmonic motions in MR elastography. *Magn Reson Med*. 2007;57(2):388-395.
31. Bernstein MA, King KF, Zhou XJ. *Handbook of MRI Pulse Sequences*. Amsterdam: Elsevier Academic Press; 2004.
32. Hogben L. *Handbook of Linear Algebra*. 2nd ed. Boca Raton, FL: Chapman and Hall/CRC; 2013.
33. Bronshtein IN, Semendyayev KA, Musiol G, Muehlig H. *Handbook of Mathematics*. Berlin, Heidelberg: Springer Berlin Heidelberg; 2007.
34. Sack I, Beierbach B, Hamhaber U, Klatt D, Braun J. Non-invasive measurement of brain viscoelasticity using magnetic resonance elastography. *NMR Biomed*. 2008;21(3):265-271.
35. Sinkus R, Tanter M, Catheline S, et al. Imaging anisotropic and viscous properties of breast tissue by magnetic resonance-elastography. *Magn Reson Med*. 2005;53(2):372-387.
36. Glaser KJ, Felmlee JP, Manduca A, Ehman RL. Shear stiffness estimation using intravoxel phase dispersion in magnetic resonance elastography. *Magn Reson Med*. 2003;50(6):1256-1265.
37. Yin Z, Kearney SP, Magin RL, Klatt D. Concurrent 3D acquisition of diffusion tensor imaging and magnetic resonance elastography displacement data (DTI-MRE): theory and in vivo application. *Magn Reson Med*. 2017;77(1):273-284.

38. Pruessmann KP, Weiger M, Scheidegger MB, Boesiger P. SENSE: Sensitivity encoding for fast MRI. *Magn Reson Med*. 1999;42(5):952-962.
39. Galil Z, Kiefer J. D-optimum weighing designs. *Ann Stat*. 1980;8(6):1293-1306.
40. Hadamard J. Résolution d'une question relative aux déterminants. *Bull Sci Math*. 1893;17:30-31.
41. Conturo TE, Smith GD. Signal-to-noise in phase angle reconstruction: dynamic range extension using phase reference offsets. *Magn Reson Med*. 1990;15(3):420-437.
42. Bernstein MA, Ikezaki Y. Comparison of phase-difference and complex-difference processing in phase-contrast MR angiography. *J Magn Reson Imaging*. 1991;1(6):725-729.
43. McGarry MDJ, Van Houten EEW, Perriñez PR, Pattison AJ, Weaver JB, Paulsen KD. An octahedral shear strain-based measure of SNR for 3D MR elastography. *Phys Med Biol*. 2011;56(13):N153-N164.
44. Papazoglou S, Xu C, Hamhaber U, et al. Scatter-based magnetic resonance elastography. *Phys Med Biol*. 2009;54(7):2229-2241.
45. Wang H, Weaver JB, Perreard II, Doyley MM, Paulsen KD. A three-dimensional quality-guided phase unwrapping method for MR elastography. *Phys Med Biol*. 2011;56(13):3935-3952.
46. Li BN, Shan X, Xiang K, et al. Evaluation of robust wave image processing methods for magnetic resonance elastography. *Comput Biol Med*. 2014;54:100-108.
47. Barnhill E, Kennedy P, Johnson CL, Mada M, Roberts N. Real-time 4D phase unwrapping applied to magnetic resonance elastography. *Magn Reson Med*. 2015;73(6):2321-2331.

How to cite this article: Guenthner C, Runge JH, Sinkus R, Kozerke S. Analysis and improvement of motion encoding in magnetic resonance elastography. *NMR in Biomedicine*. 2018;31:e3908. https://doi.org/10.1002/nbm.3908

APPENDIX A

VARIANCE AND COVARIANCE OF ESTIMATED MOTION PHASES

The measured motion phases $\varphi_k\left(\vec{x}\right)$ for each time-point k are given according to Equation 5 as

$$\vec{\varphi}_k\left(\vec{x}\right) = \hat{E}\begin{pmatrix}\vec{\phi}_k\left(\vec{x}\right)\\ \delta_k\left(\vec{x}\right)\end{pmatrix} + \vec{\eta},$$

where the phase noise $\vec{\eta}$ is assumed to be of zero mean, uncorrelated and of equal finite standard deviation σ_η for all measured encoding directions N_{Enc}. For simplicity and without loss of generality, the dependence on the wave phase offset k and position $\vec{x}$ will be omitted in the following.

The variance σ^2 of a random variable X and the covariance of the random variables X and Y are given by[33]

$$\sigma^2 = E\left[(X - E[X])^2\right] \text{ and } \mathrm{cov} = E[(X - E[X])(Y - E[Y])],$$

where E[⋯] is the expectation value operator. In the following, X and Y will be assumed to be the reconstructed target phases $\underline{\phi}_i$ with $i \in \{x, y, z, \delta\}$, which are given by

$$\vec{\underline{\phi}} = \hat{D}\vec{\varphi} = \hat{D}\left(\hat{E}\vec{\phi} + \vec{\eta}\right) = \vec{\phi} + \hat{D}\vec{\eta}\,.$$

By definition, noise is assumed to be of zero mean leading to $\mathrm{E}\left[\vec{\eta}\right] = \mathrm{E}\left[\hat{D}\vec{\eta}\right] = 0$ and the expectation value of the reconstructed phase is equal to the motion phase

$$\mathrm{E}\left[\vec{\underline{\phi}}\right] = \mathrm{E}\left[\begin{pmatrix}\vec{\phi}\\ \delta\end{pmatrix} + \hat{D}\vec{\eta}\right] = \mathrm{E}\left[\begin{pmatrix}\vec{\phi}\\ \delta\end{pmatrix}\right] + \mathrm{E}\left[\hat{D}\vec{\eta}\right] = \begin{pmatrix}\vec{\phi}\\ \delta\end{pmatrix},$$

assuming that no phase wrap occurred during the encoding process or that unwrapping was successfully applied. The calculation of the covariance matrix can be simplified to

$$\mathrm{cov}_{ij} = \mathrm{E}\left[\left(\underline{\phi}_i - \mathrm{E}\left[\underline{\phi}_i\right]\right)\left(\underline{\phi}_j - \mathrm{E}\left[\underline{\phi}_j\right]\right)\right] = \mathrm{E}\left[\left(\hat{D}\vec{\eta}\right)_i\left(\hat{D}\vec{\eta}\right)_j\right].$$

The evaluation is straightforward using the linearity of the expectation value operator and the assumption of uncorrelated and equal noise, which results in

$$\mathrm{E}\left[\eta_i\eta_j\right] = \sigma_\eta^2\delta_{ij},$$

where δ_{ij} is the Kronecker symbol. The covariance matrix elements are then given by

$$\begin{aligned} \mathrm{cov}_{ij} &= \mathrm{E}\left[\left(\widehat{D}\,\vec{\eta}\right)_i \cdot \left(\widehat{D}\,\vec{\eta}\right)_j\right] = \sum_{k,m} \widehat{D}_{ik} \cdot D_{jm}\, \mathrm{E}[\eta_k \eta_m] \\ &= \sigma_\eta^2 \sum_{k,m} \widehat{D}_{ik} \delta_{km} \widehat{D}^{\mathrm{T}}_{mj} = \sigma_\eta^2 \sum_k \widehat{D}_{ik} \widehat{D}^{\mathrm{T}}_{kj} = \sigma_\eta^2 \left(\widehat{D}\widehat{D}^{\mathrm{T}}\right)_{ij} \end{aligned},$$

whereas the variance of the reconstructed motion phases and the spurious phase offset are given by the diagonal elements

$$\sigma_i^2 = \mathrm{cov}_{ii}.$$